

Cite this: *J. Mater. Chem. C*, 2019,
7, 10881Amorphous electron donors with controllable
morphology for non-fullerene polymer solar
cells†Nergui Uranbileg,^{ab} Chenglin Gao,^{ac} Chunming Yang,^d Xichang Bao,^{id}^a
Liangliang Han^{*a} and Renqiang Yang^{id}^{*a}

The aggregation and crystallinity of polymeric donors are significant for polymer solar cells (PSCs), which dominate the film forming properties, morphology, and micro-structures of the active layer, and consequently, influence the charge carrier generation and transport in the device. Regulation of the aggregation of polymers can be realized *via* the design of alkyl chains, and thus, herein, a cyclohexylmethyl side chain is employed and grafted on PBDD-T, which is one of the most efficient polymeric donors for non-fullerene PSCs, to construct two new polymers, PBDD-CH and PBDD-CH-S. Both polymers have a high number-average molecular weight (M_n) of 50.06 kDa and 58.50 kDa, respectively, but excellent solution processability. Their optical properties indicate that PBDD-CH has a weak aggregation characteristic even at room temperature, which is caused by the steric cyclohexylmethyl side chains. Therefore, the newly designed polymers exhibit amorphous aggregation behavior in their film states, which was characterized by grazing incidence X-ray diffraction analysis. PBDD-CH and PBDD-CH-S have a similar optical bandgap (E_g^{opt}) of 1.85 eV and low lying highest occupied molecular orbital (HOMO) energy levels of -5.52 and -5.47 eV, respectively. The polymer:ITIC morphologies and phase separation could be easily controlled using 1,8-diiodooctane (DIO) and thermal annealing post-treatment, which resulted in a smooth surface morphology and well-defined phase separation, as characterized by atomic force microscopy (AFM) and transmission electron microscopy (TEM) measurements. The best power conversion efficiency (PCE) for PBDD-CH:ITIC and PBDD-CH-S:ITIC was 8.21% and 9.63%, respectively, which are rarely reported for amorphous polymer:acceptor blends.

Received 20th May 2019,
Accepted 6th August 2019

DOI: 10.1039/c9tc02663k

rsc.li/materials-c

1. Introduction

Polymer solar cells (PSCs) have attracted much attention due to their ability to be printed, large area, flexibility and low cost.^{1–3} However, their power conversion efficiency (PCE) is a bottleneck for their commercial application, which is restricted by the lack of electron donors, acceptors and understanding of the morphology of donor–acceptor bulk heterojunctions (BHJ).

Fullerene derivatives, such as phenyl-C₆₁-butyric acid methyl ester (PC₆₁BM) and its derivative PC₇₁BM, have been the dominant electron acceptors for the last decade due to their high electron mobility, large nonplanar spherical structure, and ability to form the favorable bulk heterojunction (BHJ) morphology.^{4–6} However, the low lying lowest unoccupied molecular orbital (LUMO) energy levels and weak absorption of fullerene derivatives restrict the open-circuit voltage (V_{oc}) and short-circuit current density (J_{sc}) in PSCs. Recently, non-fullerene electron acceptors (NFAs) with a low bandgap (LBG), and high absorption coefficient (ϵ) and electron mobility (m_e) have exhibited great prospect in the field of PSCs.^{7–10} In particular, small molecule electron acceptors (SMAs), which exhibit good stability, easily tuned chemical structure and low-cost production process, are likely to replace fullerene derivatives.^{11–16} The PCE of the state-of-the-art non-fullerene PSC has exceeded 15% for single-junction cells,^{17–19} and 17% for tandem cells.²⁰

Due to the rapid development of non-fullerene PSCs, much attention has been paid to wide bandgap (WBG) polymers on account of their complementary absorption with LBG SMAs in

^a CAS Key Laboratory of Bio-based Materials, Qingdao Institute of Bioenergy and Bioprocess Technology, Chinese Academy of Sciences, Qingdao 266101, China. E-mail: hanll@qibebt.ac.cn, yangrq@qibebt.ac.cn

^b Centre of Materials Science and Optoelectronics Engineering, University of Chinese Academy of Sciences, Beijing 100049, China

^c College of Materials Science and Engineering, Qingdao University of Science and Technology, Qingdao 266042, China

^d Shanghai Synchrotron Radiation Facility, Shanghai Advanced Research Institute, Chinese Academy of Sciences, Shanghai 201204, China

† Electronic supplementary information (ESI) available: GPC measurement, UV-vis absorption coefficient, charges carrier mobility, NMR spectra and HRMS spectra. See DOI: 10.1039/c9tc02663k

recent years, such as the regulation of their energy levels and bandgaps, and optimization of their self-assembly and microstructures.^{21–23} The highest occupied molecular orbital (HOMO)

energy level of polymers can be regulated *via* the electron-induced effect, for example, highly electronegative fluorine (F) and sulfur (S) atoms are widely used to control the frontier molecular orbitals of polymer,^{24,25} which can also influence their aggregation and crystalline behaviors. Moreover, once F or S atoms are introduced, the intra- and inter-molecular interactions are strengthened because of the formation of noncovalent bond action, a tightly π - π stacked polymer backbone and high degree of packing order, which are also crucial for inter-chain charge carrier transport.²⁶ However, as has been reported for some strongly aggregated or highly crystalline polymers, their phase

separation is difficult to control when blended with electron acceptors, which will influence the charge carrier generation and result in poor device performances.²⁷ Thus, the design of polymeric donors for non-fullerene PSCs is highly necessary, where not only their complementary absorption and matching energy level should be considered, but also good miscibility between the polymer and SMA. Evidence suggests that an ideal active layer should have a bicontinuous network, in which both the donor and acceptor molecules are in orderly rows in their phases.^{6,28,29}

Alkyl side chains, which are used to optimize the solution processability for semi-conducting polymers, are also employed to regulate the optical and electrical properties of polymers.³⁰

For fullerene PSCs, the structure of the polymeric donor dominates not only the absorption, but also the phase-separated morphology of the active layer. Yan *et al.* reported that the aggregation of the polymer correlated with the design of alkyl chains, where the polymer:fullerene phase structure lay on the optimized polymer structure and was independent of the fullerene structures.³¹ The type of the alkyl chain can influence the polymer backbone arrangement and orientation, and thus, the polymer:fullerene structures and photovoltaic performances.

For non-fullerene PSCs, the SMAs have a distinctive design feature, resulting in appropriate stacking, and thus the transport of electrons instead of holes. Accordingly, tailoring the structure of SMAs may lead to significant changes in their aggregation, crystallinity, and film micro-structures, which will affect the polymer:SMA phase separation. Therefore, the donor selectivity of SMAs will be different from that of fullerene derivatives.

However, only a few studies have focused on the optimization of the polymeric donor aggregation to better match with SMAs for non-fullerene PSCs. Benzo[1,2-*c*:4,5-*c'*]dithiophene-4,8-dione (BDD)^{32–34} and 5,6-difluoro-2*H*-benzo[*d*][1,2,3]triazole (ffTAZ)^{35–37} alternating benzo[1,2-*b*:4,5-*b'*]dithiophene (BDT) polymer are the most well-known WBG polymers that match well with SMAs. Our previous work demonstrated that optimizing the aggregation of BDT–ffTAZ can promote the miscibility of polymer:SMA, and

realize nearly an ideal active layer morphology and microstructure in the absence of any post-treatment.²¹ The BDD and BDT alternating polymer PBDB-T has a rigid and planar backbone, which to date, is one of the most efficient polymeric donors for non-fullerene PSCs. However, the HOMO energy level of PBDB-T is relatively high, and resulting in a low V_{OC} of around

0.9 V when blended with 3,9-bis(2-methylene-(3-(1,1-dicyanomethylene)-indanone))-5,5,11,11-tetrakis(4-hexylphenyl)-dithieno[2,3-*d*:2',3'-*d'*]-*s*-indaceno[1,2-*b*:5,6-*b'*]dithiophene (ITIC).³⁸ Accordingly, F and S atoms have been introduced to enlarge the V_{OC} ; however, the enhanced inter-chain interaction makes it difficult to balance the solution processability and molecular weight. In this work, a steric cyclohexylmethyl side chain was employed to adjust the energy level and aggregation of a BDD-based polymer. Two polymers PBDD-*CH* and PBDD-*CH*-S were designed and synthesized, and our results demonstrate the bulky side chains significantly decreased the HOMO energy level of the polymers, resulting in a higher V_{OC} of 0.98 V for the as-cast PBDD-*CH*:ITIC and PBDD-*CH*-S:ITIC solar cells. Interestingly, PBDD-*CH* and PBDD-*CH*-S exhibit weak aggregation behavior, and are relatively amorphous in their pristine and blend film states. However, the polymer:ITIC blends show excellent photovoltaic performances with a PCE of 8.21% and 9.63%, respectively, which are rarely reported for amorphous polymers and acceptors. Thus, we propose that steric alkyl chains are effective substituents to regulate the energy levels of polymers and balance their molecular weight and solution processability, finally resulting in easily controlled polymer:SMA morphologies and phase-separated structures.

2. Experimental

2.1. General information

Common reagent grade solvents including deuterated chloroform ($CDCl_3$), anhydrous chlorobenzene (CB, 99.8%) and *o*-dichlorobenzene (*o*-DCB) were purchased from Sigma-Aldrich and used without further treatment. Tetrahydrofuran (THF) and toluene were carefully dried and distilled from appropriate drying agents prior to use. 1,3-Dibromo-5,7-bis(2-ethylhexyl)-benzo[1,2-*c*:4,5-*c'*]dithiophene-4,8-dione, 2,6-bis(trimethyltin)-4,8-bis(5-(2-ethylhexyl)thiophen-2-yl)benzo[1,2-*b*:4,5-*b'*]dithiophene, and 2,6-bis(trimethyltin)-4,8-bis(5-(2-ethylhexylthio)thiophen-2-yl)benzo[1,2-*b*:4,5-*b'*]dithiophene were purchased from SunaTech Inc. Commercially available reagents 3-bromothiophene, (bromomethyl)cyclohexane, *n*-butyllithium (1.6 M in hexane), tributyltin chloride, tetra-*n*-butylammonium hexafluorophosphate (*n*- Bu_4NPF_6), tris(dibenzylideneacetone)dipalladium ($Pd_2(dba)_3$) and tri(*o*-tolyl)phosphine ($P(o-tol)_3$) were purchased from Aladdin and Sigma-Aldrich and used without further purification unless otherwise stated. Indium tin oxide (ITO)-coated glass substrates with a sheet resistance of $10 \Omega \text{ cm}^{-1}$ were obtained from Shenzhen Display Inc. (China). PDINO and ITIC were purchased from Derthon Optoelectronic Materials and PEDOT:PSS (CleviosTM PVP. Al 4083) was obtained from Heraeus Materials Technology Ltd. Nuclear magnetic resonance (NMR) spectra were measured in $CDCl_3$ on a Bruker AVANCE 600 MHz Fourier transform NMR spectrometer, and chemical shifts were quoted relative to the internal standard tetramethylsilane (TMS). High-resolution mass spectroscopy (HRMS) experiments were performed on a 15 T SolariX XR Fourier transform ion cyclotron resonance (FTICR) spectrometer (Bruker Daltonics, Bremen, Germany) coupled with a standard APPI source. The molecular

weights of the polymers were measured *via* gel permeation chromatography (GPC) performed on a PL-GPC 220 (Agilent), and polystyrene was used as the standard (150 IC, 1,2,4-trichlorobenzene (TCB) as the eluent). Absorption spectra were recorded with a Hitachi U-4100 UV-vis-NIR scanning spectrophotometer. Cyclic voltammetry (CV) measurements were performed on a CHI660D electrochemical workstation equipped with a three-electrode cell consisting of a glassy carbon working electrode, saturated calomel electrode (SCE) reference electrode and platinum wire counter electrode. The measurements were carried out in anhydrous acetonitrile containing 0.1 M *n*-Bu₄NPF₆ as the supporting electrolyte under an argon atmosphere at a scan rate of 100 mV s⁻¹. Thin films were deposited from chloroform solution onto the working electrodes and dried under nitrogen prior to the measurement. The redox potential of the Fc/Fc⁺ internal reference was 0.40 V vs. SCE. The HOMO and LUMO energy levels were calculated using the empirical formula of $E_{\text{HOMO}} = -e(E_{\text{ox}} + 4.4 - E_{(\text{Fc}/\text{Fc}^+)})^{1/2}$ and $E_{\text{LUMO}} = E_{\text{HOMO}} + E_{\text{g}}^{\text{opt}}$, where E_{ox} and $E_{\text{g}}^{\text{opt}}$ are the onset oxidation potential and the optical bandgap, respectively. Atomic force microscopy (AFM) images were acquired using an Agilent-5400 scanning probe microscope with a Nanodrive controller in tapping mode with MikroMasch NSC-15 AFM tips with resonant frequencies of B300 kHz. Bright-field transmission electron microscopy (TEM) images were acquired using a HITACHI H-7650 electron microscope operating at an acceleration voltage of 100 kV. Grazing incidence wide-angle X-ray scattering (GIWAXS) patterns were acquired by beamline BL16B1 (Shanghai Synchrotron Radiation Facility). The X-ray wavelength was 0.124 nm ($E = 10$ keV), and the incidence angle was set to 0.21.

2.2. Synthesis of the monomer and polymers

1,3-Bis(4-(cyclohexylmethyl)thiophen-2-yl)-5,7-di(2-ethylhexyl)benzo[1,2-*c*:4,5-*c'*]-dithiophene-4,8-dione. Under an argon atmosphere, 1,3-dibromo-5,7-bis(2-ethylhexyl)benzo[1,2-*c*:4,5-*c'*]-dithiophene-4,8-dione (0.60 g, 1 mmol), tributyl(4-(cyclohexylmethyl)thiophen-2-yl)stannane (1.41 g, 3 mmol), Pd₂(dba)₃ (18.3 mg, 0.02 mmol) and P(*o*-tol)₃ (36.5 mg, 0.12 mmol) were mixed in a 50 mL flask, and then 20 mL dry toluene was added. The mixture was refluxed overnight, then cooled to room temperature, and the solvent was evaporated under reduced pressure. The crude product was purified by silica gel column chromatography (eluent: petroleum ether/CH₂Cl₂ = 10 : 1, v/v) and dried under vacuum to provide 1,3-bis(4-(cyclohexylmethyl)thiophen-2-yl)-5,7-di(2-ethylhexyl)benzo[1,2-*c*:4,5-*c'*]-dithiophene-4,8-dione as a yellow solid (yield = 93.6%, 0.75 g). ¹H NMR (400 MHz, CDCl₃): δ (ppm) 7.56 (s, 2H), 7.06 (s, 2H), 3.36–3.25 (m, 4H), 2.51 (d, *J* = 4 Hz, 4H), 1.77–1.63 (m, 12H), 1.41–1.12 (m, 24H), 1.00–0.83 (m, 16H). ¹³C NMR (101 MHz, CDCl₃): δ 177.74, 153.14, 142.63, 141.84, 133.18, 132.88, 132.36, 132.28, 125.35, 41.22, 39.15, 38.40, 33.63, 33.19, 32.76, 28.80, 26.94, 26.54, 26.31, 26.02, 23.04, 22.68, 14.14, 10.90.

1,3-Bis(5-bromo-4-(cyclohexylmethyl)thiophen-2-yl)-5,7-di(2-ethylhexyl)benzo[1,2-*c*:4,5-*c'*]-dithiophene-4,8-dione. 1,3-Bis(4-(cyclohexylmethyl)thiophen-2-yl)-5,7-di(2-ethylhexyl)benzo[1,2-*c*:4,5-*c'*]-dithiophene-4,8-dione (0.40 g, 0.5 mmol) was added to

a dry two-neck 20 mL round-bottom flask, the flask was charged with nitrogen, and then 5 mL chloroform and 1 mL acetic acid were added sequentially. The reaction mixture was stirred in the dark, and then *N*-bromosuccinimide (NBS) (0.18 g, 1 mmol) was added within 5 min. Afterwards, the reaction mixture was monitored by TLC until the starting material was consumed. Then 10 mL deionized water was added and the product extracted with dichloromethane three times, and the organic phase was combined and washed with water, then dried using anhydrous sodium sulfate. After removing the solvent, the crude product was purified by silica gel column chromatography (eluent: petroleum ether/CH₂Cl₂ = 15 : 1, v/v) and dried under vacuum to provide 1,3-bis(5-bromo-4-(cyclohexylmethyl)thiophen-2-yl)-5,7-di(2-ethylhexyl)benzo[1,2-*c*:4,5-*c'*]-dithiophene-4,8-dione as a yellow solid, which was recrystallized from a mixture of ethanol and tetrahydrofuran as a yellow powder (yield = 79.2%, 0.38 g). ¹H NMR (600 MHz, CDCl₃): δ (ppm) 7.37 (s, 2H), 3.34–3.26 (m, 4H), 2.48 (d, 4H), 1.77–1.65 (m, 12H), 1.43–1.16 (m, 24H), 1.04–0.98 (m, 4H), 0.94–0.89 (m, 12H). ¹³C NMR (150 MHz, CDCl₃): δ (ppm) 147.99, 147.86, 146.31, 146.18, 141.18, 137.18, 131.66, 131.47, 113.74, 109.42, 109.35, 59.85, 39.09, 38.77, 37.20, 33.12, 31.93, 31.88, 31.54, 29.90, 29.64, 29.58, 29.35, 26.49, 26.41, 26.36, 26.28, 22.70, 14.14, 14.12. ¹³C NMR (151 MHz, CDCl₃) δ 177.60, 153.74, 141.66, 140.79, 132.74, 132.57, 131.90, 131.52, 116.17, 41.20, 38.76, 37.14, 33.67, 33.11, 32.82, 29.72, 28.88, 26.46, 26.25, 26.05, 23.05, 14.21, 10.89. HRMS (APPI): *m/z* calcd for C₄₈H₆₂Br₂O₂S₄: 956.19994; found: 956.19961.

Synthesis of polymers

The polymers were synthesized according to a previous report.³⁹ 2,6-Bis(trimethyltin)-4,8-bis(5-(2-ethylhexyl)thiophen-2-yl)benzo[1,2-*b*:4,5-*b'*]-dithiophene or 2,6-bis(trimethyltin)-4,8-bis(5-(2-ethylhexylthio)thiophen-2-yl)benzo[1,2-*b*:4,5-*b'*]-dithiophene (0.2 mmol), 1,3-bis(5-bromo-4-(cyclohexylmethyl)thiophen-2-yl)-5,7-di(2-ethylhexyl)benzo[1,2-*c*:4,5-*c'*]-dithiophene-4,8-dione (0.2 mmol), Pd₂(dba)₃ (1.8 mg, 0.002 mmol) and P(*o*-tol)₃ (3.6 mg, 0.012 mmol) were dissolved in 6 mL toluene in a 25 mL round-bottom flask protected by argon. The flask was purged three times with successive vacuum and argon filling cycles. The oil bath was heated to 110 °C gradually, and the reaction mixture was stirred for 18 h at 110 °C under an argon atmosphere. After cooling, the mixture was cooled to room temperature and precipitated in 200 mL methanol. The precipitate was filtered and washed with methanol and hexane successively in a Soxhlet apparatus to remove the oligomers and catalyst residue. Finally, the polymer was extracted with chloroform. The chloroform fraction was concentrated and precipitated in methanol. The precipitate was filtered and dried under vacuum at 40 °C overnight.

PBDD-CH, black solid, GPC: number-average molecular weight (M_n) = 50.05 kDa, polydispersity index (PDI) = 1.98. ¹H NMR (600 MHz, CDCl₃): δ (ppm) 7.71–7.65 (br, ArH), 7.62–7.51 (br, ArH), 7.34–7.28 (br, ArH), 6.90–6.82 (br, ArH), 3.35–3.12 (br, CH₂), 2.86–2.78 (br, CH₂), 2.75–2.63 (br, CH₂), 1.80–1.56 (br, CH), 1.42–1.06 (br, CH₂), 0.93–0.75 (br, CH₃).

PBDD-CH-S, GPC: $M_n = 58.50$ kDa, PDI = 2.25. ^1H NMR (600 M Hz, CDCl_3): δ (ppm) 7.72–7.68 (br, ArH), 7.67–7.63 (br, ArH), 7.44–7.39 (br, ArH), 7.25–7.23 (br, ArH), 3.42–3.21 (br, CH_2), 3.10–2.93 (br, CH_2), 2.81–2.70 (br, CH_2), 1.81–1.61 (br, CH), 1.47–1.17 (br, CH_2), 1.00–0.78 (br, CH_3).

2.3. Device fabrication and evaluation

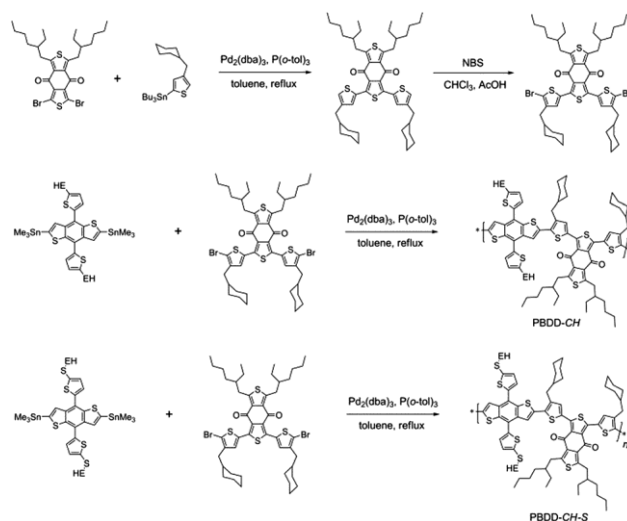
The devices were fabricated with the configuration of ITO/PEDOT:PSS/polymer:SMA/PDINO/Al.²³ The ITO-coated substrates were cleaned with detergent, deionized water, acetone and isopropyl alcohol in an ultrasonic bath sequentially for 15 min, and dried under ultra-pure N_2 and then treated with O_2 plasma for 6 min. Then, a 30 nm PEDOT:PSS layer was spin-cast on the ITO-coated glass at 4000 rpm and baked at 150 °C for 20 min in an oven, and then the substrates were transferred to a glovebox filled with N_2 . CB solutions consisting of the polymers and SMA in different blend ratios were stirred overnight at room temperature (the optimized polymer concentrations for PBDD-CH and PBDD-CH-S were 8 and 10 mg mL^{-1} , respectively). The above solution was spin-coated to form the active layer on the ITO/PEDOT:PSS substrate, and the optimized thicknesses of the PBDD-CH/ITIC and PBDD-CH-S/ITIC films were B130 and B148 nm, respectively, which were estimated using a Veeco Dektak 150 surface profiler. Subsequently, an ultrathin layer of PDINO (0.2 mg mL^{-1} in methanol) was cast on the active layer at 2600 rpm for 20 s. Finally, an Al (100 nm) metal electrode was thermally evaporated under about 4×10^{-4} Pa and the device area was defined by a shadow mask as 0.1 cm^2 .

The current density–voltage (J - V) characteristics of the devices were recorded using a Keithley 2420 source measurement unit under the illumination of AM 1.5G (100 mW cm^{-2} , Newport solar simulator). The light intensity was calibrated with a standard silicon solar cell. The external quantum efficiencies (EQE) of the solar cells were analyzed using a certified Newport incident photon conversion efficiency (IPCE) measurement system. The hole-only device employed a device architecture of ITO/PEDOT:PSS/active layer/ MoO_3 /Al and the electron-only device employed a device architecture of ITO/ ZnO /active layer/PDINO/Al, and the related thicknesses of the active layers were determined using a Dektak 150 surface profiler. Mobility was measured using the space-charge-limited current (SCLC) method, which fits the J - V curve with a space charge limited form, where the SCLC is described by $J = 9\epsilon_0\epsilon_r m_h(e) V^2 / 8d^3$,⁴⁰ where ϵ_0 is the permittivity of free space (8.85×10^{-12} F m^{-1}), ϵ_r is the relative permittivity of the material (assumed to be 3), m_h is the hole mobility and m_e is the electron mobility. $V = V_{\text{appl}} - V_{\text{bi}} - V_s$ (V_{appl} is the applied voltage, V_{bi} is the built-in voltage, and V_s is the voltage drop from the substrates series resistance) and d is the thickness of the related films.

3. Results and discussion

3.1. Synthesis

PBDD-CH and PBDD-CH-S were prepared *via* Pd(0)-catalyzed Stille polymerization, as described in Scheme 1. Both polymers



Scheme 1 Synthetic routes for the monomers and polymers.

exhibited a red solution in refluxing toluene, but a viscous dark solution when cooled to room temperature, which precipitated from methanol as continuous fibers with metallic luster, indicating their potential high molecular weight. PBDD-CH and PBDD-CH-S exhibited excellent solubility in common solvents such as chloroform (CF), chlorobenzene (CB) and *o*-dichlorobenzene (*o*-DCB) at room temperature. The M_n of PBDD-CH and PBDD-CH-S is 50.06 kDa and 58.50 kDa with PDI of 1.98 and 2.25, respectively, which were measured *via* gel permeation chromatography (GPC) using TCB as the eluent at 150 °C (Table 1 and Fig. S1 in the ESI†).

3.2. Photophysical and electrochemical properties

The UV-vis absorption spectra for PBDD-CH and PBDD-CH-S are shown in Fig. 1 and summarized in Table 1. Both the polymers have a similar E_g^{opt} of about 1.85 eV in their thin-film state, which is comparable to that of PBDB-T. However, as shown in Fig. 1, PBDD-CH shows a hypsochromic absorption in CB solution, with an absorption peak at 520.25 nm together with a weak shoulder peak at 616.14 nm, indicating the π - π stacking in PBDD-CH is strongly hindered by its bulky side chains. The dilute PBDD-CH solution exhibited a red rather than a dark solution compared with PBDD-CH-S, which also implies its weak aggregation characteristic. This weak aggregation behavior is approximately ascribed to the tortuous polymer backbone. For PBDD-CH-S, similar absorption profiles were observed for its solution and film states, showing two absorption peaks centered at 582.08 nm and 627.50 nm, respectively, indicating the introduction of S atoms enhanced the intermolecular interactions. PBDD-CH and PBDD-CH-S have relatively high ϵ of 6.9×10^4 and 7.9×10^4 cm^{-1} in their film states, respectively (Fig. S2, ESI†), and their absorption is complementary with that of ITIC, as shown in Fig. 1, which possesses a low E_g^{opt} of 1.49 eV.

Electrochemical cyclic voltammetry (CV) measurements were performed to determine the HOMO and LUMO levels of PBDD-CH and PBDD-CH-S. As shown in Fig. 2, only oxidation

Table 1 Summary of the photophysical and electrochemical properties of the PBDD-CH and PBDD-CH-S polymers

Polymer	M_n (kDa)	M_w (kDa)	PDI	ϵ (cm^{-1})	l_{edge} (nm)	E_g^{opt} (eV)	E_{ox} (V)	E_{HOMO} (eV)	E_{LUMO} (eV)
PBDD-CH	50.06	99.17	1.98	6.9×10^4	670	1.85	1.12	-5.52	-3.67
PBDD-CH-S	58.50	131.76	2.25	7.9×10^4	672	1.85	1.07	-5.47	-3.62

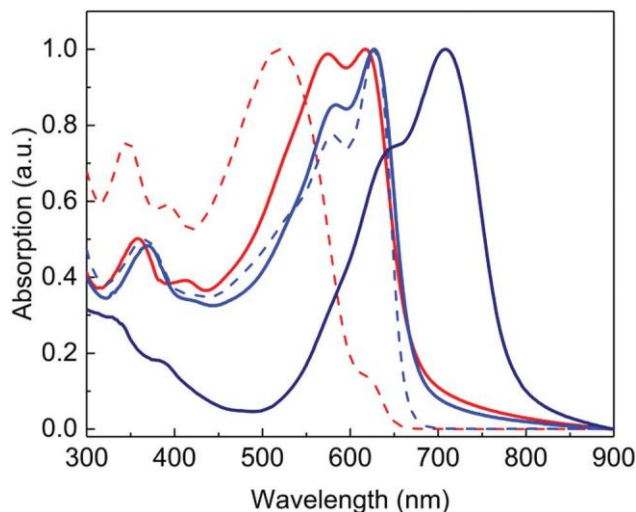


Fig. 1 UV-vis absorption of PBDD-CH (red) and PBDD-CH-S (blue) in CB solution (dash line) and thin-film state (solid line), and UV-vis absorption of pristine ITIC (navy) film.

potentials were observed for both polymers. PBDD-CH and PBDD-CH-S exhibited high onset oxidation potentials (E_{ox}) at 1.12 V and 1.07 V vs. saturated calomel, and consequently, deep HOMO energy levels (E_{HOMO}) of -5.52 and -5.47 eV (Fig. 2b), respectively, which are much deeper than that of PBDB-T (-5.23 eV).⁴¹ Thus, these results indicate that the steric side chains decreased the E_{HOMO} of the polymer, which is in agreement with our previous work. In the absence of the reduction potentials, the LUMO energy level (E_{LUMO}) of PBDD-CH and PBDD-CH-S were calculated from the optical E_g and E_{HOMO} according to the formula $E_{\text{LUMO}} = E_g^{\text{opt}} + E_{\text{HOMO}}$. As summarized in Table 1, both the E_{HOMO} and E_{LUMO} decreased for compared to that of PBDB-T, where the deeper energy levels for the

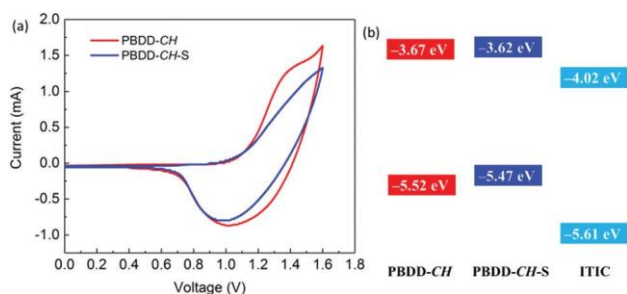
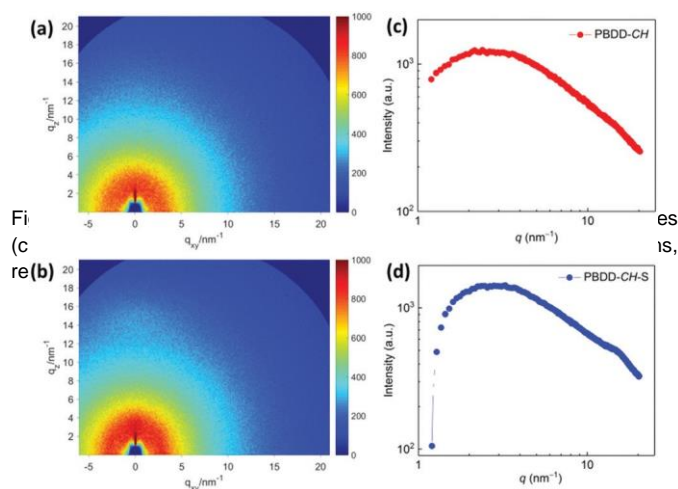


Fig. 2 CV curves of the PBDD-CH and PBDD-CH-S polymers vs. the saturated calomel electrode (a) and energy level diagrams for the polymeric donors and ITIC (b).

polymeric donor are likely to enhance the V_{OC} and diminish the energy loss (E_{loss}) for PSCs.^{42,43}

3.3. Micro-structures

Two-dimensional grazing incidence wide-angle X-ray scattering (2D-GIWAXS) was used to investigate the micro-structures of the polymer films, as depicted in Fig. 3. Unexpectedly, both polymers exhibited extremely weak crystalline characteristics compared to the reference polymer PBDB-T. Considering the difference in the design of the polymers, the relative amorphous characteristics of PBDD-CH and PBDD-CH-S are ascribed to the introduction of the steric cyclohexylmethyl side chains, which may make the polymer backbone more tortuous and hinder side-chain packing and main-chain p-p stacking. However, according to previous works, the bulky side chain is proven to be a predominant substituent that can adjust the polymer crystallinity and result in an overall compact packing.²¹ We infer this is because BDD-based polymers have relatively weak aggregation characteristics compared to other polymers such as fTAAZ- and 5,6-difluorobenzo[c][1,2,5]thiadiazole-based⁴⁴ polymers. Consequently, an appropriate distortion of the polymer backbone is favorable for the equilibrium of the crystallinity and solution processability, resulting in high photovoltaic performances.⁴⁵ Here, for the BDD-based polymers, possibly a planar backbone is more desirable for high crystallinity. An inconspicuous 010 diffraction centered at 15.01 nm^{-1} was observed for PBDD-CH-S in the out-of-plane direction, as shown in Fig. 3b and d, and the corresponding p-p stacking distance was calculated to be 4.19 \AA , which is larger than that of the reported BDD-based polymers.⁴⁶



This result indicates that the cyclohexylmethyl side chain influenced not only the degree of crystallinity, but also the molecular arrangement compactness of the polymers. This molecular-dependent micro-structure will be interesting to help understand the polymer structure–device property relationship for PSCs.

3.4. Photovoltaic properties

Considering the complementary absorption and matched energy levels of ITIC with PBDD-CH and PBDD-CH-S, ITIC was chosen as the electron acceptor to characterize the photovoltaic performances. The conventional device configuration of ITO (indium tin oxide)/PEDOT:PSS (poly(3,4-ethylenedioxythiophene)-polystyrene sulfonate)/polymer:ITIC/PDINO/Al was employed, and the detailed fabrication is provided in the Experimental section. The optimized concentration of PBDD-CH and PBDD-CH-S was 8 mg mL^{-1} and 10 mg mL^{-1} in CB, respectively, with a donor:acceptor ratio of 1 : 1 wt%, as summarized in Table 2. The as-cast PBDD-CH:ITIC and PBDD-CH-S:ITIC cells had a high V_{OC} of 0.98 V, which is about 0.1 V higher than that of the PBDD-T:ITIC-based device, with a small E_{loss} ($E_g - eV_{OC}$) of 0.59 eV. The improvement in V_{OC} is ascribed to the deeper E_{HOMO} of the polymers, which is caused by the introduction of the bulky cyclohexylmethyl side chains. The current density–voltage ($J-V$) curves of the PBDD-CH:ITIC- and PBDD-CH-S:ITIC-based devices (100 mW cm^{-2} (AM 1.5G) irradiation) are shown in Fig. 4. The PCE of 6.15% for the as-cast PBDD-CH:ITIC device is relatively low because of its low J_{SC} of 11.89 mA cm^{-2} and FF of

52.81%. Interestingly, when 0.2% DIO was added and the blend film was thermally annealed (TA) at 120 °C for 10 min, the PCE reached up to 8.21%, combined with a V_{OC} of 0.95 V, J_{SC} of 14.32 mA cm^{-2} and FF of 60.17%. The significantly improved device performances indicate the morphology and the phase separation of the polymer:ITIC blend is controllable, which is probably related to the weak aggregation characteristic of PBDD-CH. For PBDD-CH-S:ITIC, the as-cast device exhibited a moderate PCE of 8.96%, and its J_{SC} of 14.87 mA cm^{-2} and FF of 61.38% are much higher than that of the PBDD-CH:ITIC-based device. It should be noted that for most BDT-containing polymers, the alkylthio side chain can form $p_p(C)-d_p(S)$ orbital overlap between the sulfur atom and the conjugated side chain, thus decreasing the E_{HOMO} of the polymer, resulting in a higher V_{OC} .²³ However, in this work, the energy levels and V_{OC} for PBDD-CH and PBDD-CH-S are comparable. One possibility is because of the tortuous polymer backbone, which makes the frontier molecular orbital distribution more localized, and thus the electron-induced effect of the sulfur atom is not predominant compared to the steric hindrance effect of the side chains. Nevertheless, the alkylthio side chains are favorable for the polymer backbone aggregation and crystallinity, which result in high photovoltaic performances. The PCE for PBDD-CH-S:ITIC was further optimized up to 9.63% when 0.1% DIO was added and it was thermally annealed at 120 °C for 10 min, and both the FF and J_{SC} were higher than that of the optimized PBDD-CH:ITIC-based devices. All the devices exhibited a wide range

Table 2 Photovoltaic performance of the devices based on PBDD-CH:ITIC and PBDD-CH-S:ITIC

Device	D/A ratio	V_{OC} (V)	J_{SC} (mA cm^{-2})	FF (%)	PCE (%)	m_b ($\text{cm}^2 \text{V}^{-1} \text{s}^{-1}$)	m_e ($\text{cm}^2 \text{V}^{-1} \text{s}^{-1}$)
PBDD-CH:ITIC ^a	1 : 1	0.98	11.89 (10.99)	52.81	6.15	No	No
PBDD-CH:ITIC ^b	1 : 1	0.95	14.32 (13.64)	60.17	8.21	9.57×10^{-5}	1.55×10^{-4}
PBDD-CH-S:ITIC ^a	1 : 1	0.98	14.87 (14.53)	61.38	8.96	No	No
PBDD-CH-S:ITIC ^c	1 : 1	0.96	15.24 (14.73)	65.83	9.63	1.24×10^{-4}	3.06×10^{-4}

^a As-cast. ^b 0.2% DIO and thermally annealed at 120 °C for 10 min. ^c 0.1% DIO and thermally annealed at 120 °C for 10 min.

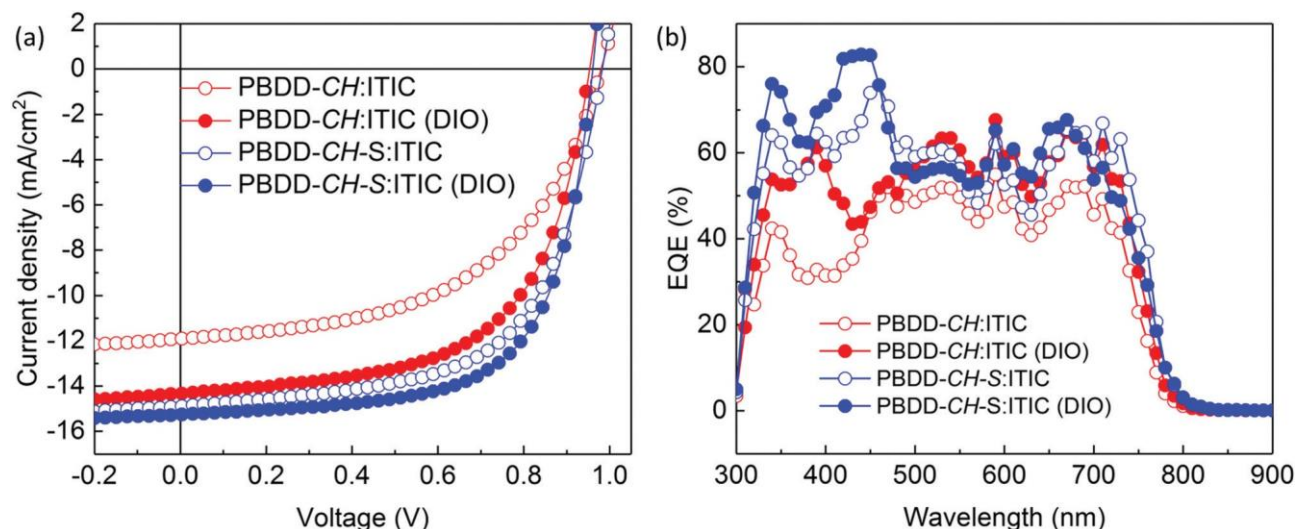


Fig. 4 $J-V$ (a) and EQE (b) curves of the as-cast and optimized polymer:ITIC devices.

spectral response from 300–800 nm, as seen from the external quantum efficiency (EQE) curves (Fig. 4b), and the J_{SC} integrated from the EQE agrees well with the measured data, as summarized in Table 2. The charge carrier mobility of the PSCs was measured using the space-charge-limited current (SCLC) method (details are provided in the Experimental section). The J – V curves of the hole-only and electron-only devices are shown in Fig. S3 (ESI†). As summarized in Table 2, the PBDD-CH:ITIC device has a hole mobility (m_h) of $9.57 \times 10^{-5} \text{ cm}^2 \text{ V}^{-1} \text{ s}^{-1}$ and electron mobility (m_e) of $1.55 \times 10^{-4} \text{ cm}^2 \text{ V}^{-1} \text{ s}^{-1}$, and their m_h is relatively lower than that of reported BDD-based polymers, which maybe because of the weak crystallinity of PBDD-CH. The m_h of $1.24 \times 10^{-4} \text{ cm}^2 \text{ V}^{-1} \text{ s}^{-1}$ and m_e of $3.06 \times 10^{-4} \text{ cm}^2 \text{ V}^{-1} \text{ s}^{-1}$ for PBDD-CH-S:ITIC are higher than that of PBDD-CH:ITIC, which are favorable for the reduction of exciton recombination and FF.

The plots of photocurrent density (J_{ph}) versus the effective applied voltage (V_{eff}) are depicted in Fig. 5a, which were used to characterize the exciton dissociation and charge collection of the optimized devices.⁴⁷ The effective experimental photocurrent density is given by $J_{ph} = J_L - J_D$, where J_L and J_D are the photocurrent densities under illumination and in the dark, respectively. V_{eff} is given by $V_{eff} = V_0 - V_{appl}$, where V_0 is defined as the voltage, where $J_L = J_D$ and V_{appl} is the applied bias.⁴⁸ J_{ph} is plotted on a double logarithmic scale against the V_{eff} . For PBDD-CH:ITIC, J_{ph} is saturated at $V_{eff} \approx 1.5$ V, and the saturated photocurrent density (J_{sat}) is 14.67 mA cm^{-2} ; therefore, the charge extraction probability (J_{ph}/J_{sat}) was estimated to be as high as 97.6% under short-circuit conditions. For PBDD-CH-S:ITIC, J_{ph} is saturated at $V_{eff} \approx 1.5$ V, and J_{sat} is 15.70 mA cm^{-2} , resulting in a J_{ph}/J_{sat} of 97.1% under short-circuit conditions. The high charge extraction probabilities indicate sufficient exciton dissociation and effective charge collection in both devices. The J_{ph} saturated at a large bias suggests that the mean electron and hole drift lengths are equal to or larger than the device thickness and no recombination occurred. The effective exciton

dissociation and charge collection indicate good miscibility between the polymeric donors and ITIC, the morphology and phase separation of which can be easily controlled by using conventional pre- or post-treatment technologies. We also investigated the variation in J_{SC} as a function of light intensity (P_{light}) to gain deeper insight into the charge recombination using the power-law equation $J_{SC} \propto P_{light}^\alpha$,⁴⁹ where if the power-law exponent α is close to 1, it indicates weak bimolecular recombination. The J_{SC} plots versus P_{light} in the log–log scale are shown in Fig. 5b. Accordingly, the α values were deduced from the slope of the linear fitting curves to be 0.99 and 0.98 for the PBDD-CH:ITIC and PBDD-CH-S:ITIC devices, respectively, indicating negligible bimolecular recombination. These physical experiments provide strong evidence for high exciton dissociation probability and charge collection efficiency as well as effective charge recombination supersession in our solar cells.

3.4. Morphologies and phase separation

The 2D-GIWAXS profiles of the PBDD-CH:ITIC and PBDD-CH-S:ITIC films are shown in Fig. S4 (ESI†). However, there was no obvious diffraction peak observed for both films. Although ITIC is a famous electron acceptor, it is less crystalline and even amorphous when blended with some polymeric or small molecule donors.⁵⁰ Also, because of their tortuous polymer backbones, PBDD-CH and PBDD-CH-S also exhibit amorphous characteristics in the blend films. The surface micro-structures of the blend films were characterized via atomic force microscopy (AFM), and as shown in Fig. 6, it is obvious that both polymers show desirable film-forming properties and decent miscibility with the electron acceptor ITIC, whether additive was used or not. As depicted in Fig. 6a, PBDD-CH:ITIC exhibited a smooth and uniform surface morphology with a small root-mean-square (RMS) surface roughness of 0.77 nm, and when DIO was added and TA employed, the uniform surface morphology was also observed with an increased RMS of 1.24 nm (Fig. 6b). A rougher surface morphology indicates

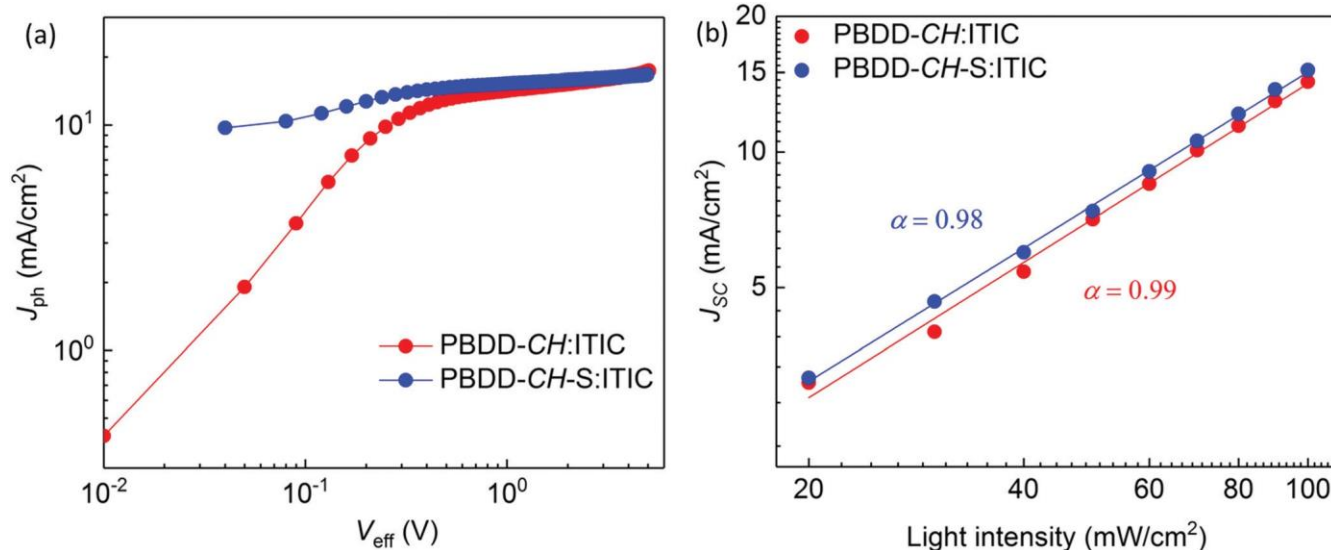


Fig. 5 J_{ph} – V_{eff} curves (a) and J_{sc} – P_{light} (b) curves for the optimized PBDD-CH:ITIC and PBDD-CH-S:ITIC devices.

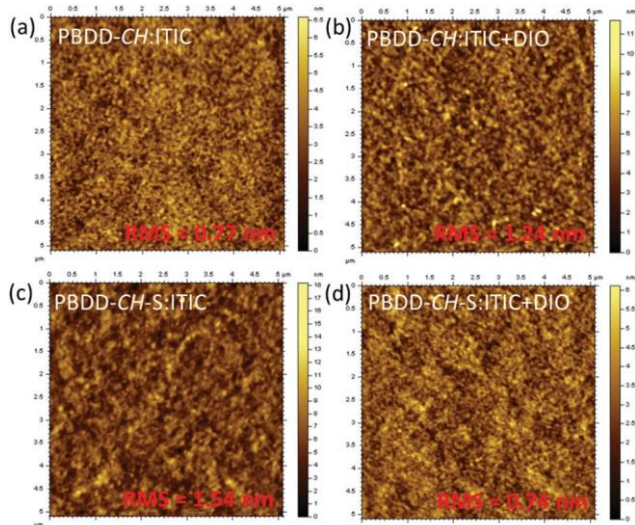


Fig. 6 AFM height images for the PBDD-CH:ITIC- and PBDD-CH-S:ITIC-based devices.

stronger aggregation of the polymer, implying that the self-assembly of PBDD-CH can easily be controlled by using post-treatment technologies. For PBDD-CH-S:ITIC, the opposite phenomenon was observed, where the as-cast blend has a rougher surface structure with RMS of 1.54 nm (Fig. 6c); nevertheless, it became smoother with an RMS of 0.74 nm (Fig. 6d) using DIO additive and TA treatment. The difference in the surface micro-structures for the active layers should be related to the distinguishing aggregation characteristics of PBDD-CH and PBDD-CH-S. However, interestingly, both optimized active layers exhibited clearly defined micro-structures, as seen from

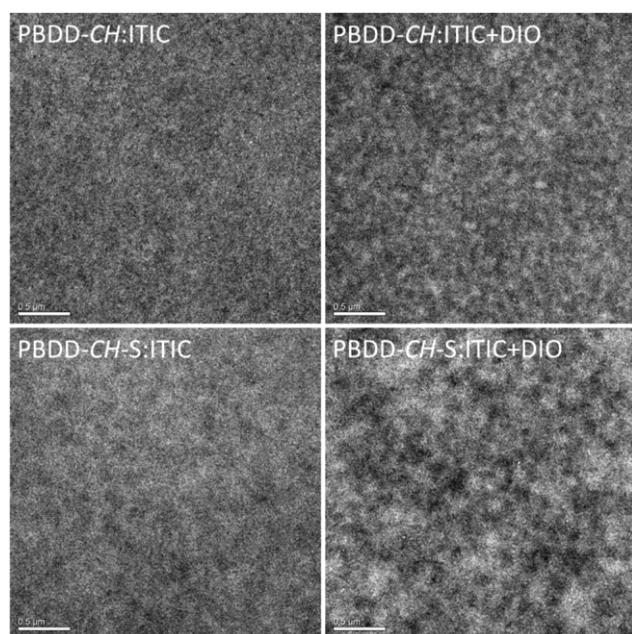


Fig. 7 TEM images of the PBDD-CH:ITIC- and PBDD-CH-S:ITIC-based devices.

the TEM images shown in Fig. 7, although both polymers have different aggregation and film forming properties. The well-defined polymer:ITIC phase separation can help explain the enhanced device performances when DIO and TA were employed. The surface and phase structures of the polymer:ITIC blends are critical for the physical processes occurring as the devices start to work, such as charge carrier generation, transport and collection. Even though the amorphous micro-structures may not be desirable for the charge carrier transport, the design of the polymeric donor to promote the donor:acceptor miscibility is surely significant for understanding the delicate polymer-SMA molecular compatibility.

4. Conclusions

In summary, two BDT and BDD alternating polymers, PBDD-CH and PBDD-CH-S, were designed and synthesized, with the aim to adjust the energy levels and aggregation characteristics of the polymers, and investigate their application for non-fullerene PSCs. Our results demonstrate that the aggregation and crystalline behaviors of BDD-BDT are significantly affected by inserting bulky cyclohexylmethyl side chains, and simultaneously, the energy levels of the polymer decreased to certain degree. Therefore, PBDD-CH and PBDD-CH-S exhibited nearly amorphous states in their pristine and blend films, but excellent film-forming properties and polymer:ITIC phase separation structures. Additionally, the V_{OC} was enhanced to 0.98 V for the as-cast PBDD-CH:ITIC- and PBDD-CH-S:ITIC-based devices. When DIO was used as an additive and thermal annealing post-treatment was employed, the PBDD-CH:ITIC and PBDD-CH-S:ITIC blend films exhibited different phase separation structures, which result in effective exciton dissociation, electron collection and diminished charge recombination. The best PCEs reached up to 8.21% and 9.63% for PBDD-CH:ITIC and PBDD-CH-S:ITIC, respectively, and although their active layers were amorphous, efficient charge carrier transport occurred. Our study indicates the aggregation and crystallinity of BDD-BDT can be easily adjusted by the side chain, which ensures good solution processability and high molecular weight. More importantly, the side chain can significantly promote the polymer:ITIC miscibility, and result in a well-controlled morphology. These results will help to understand the structure-property relationship for non-fullerene PSCs. Moreover, we conclude this strategy will be more effective for other polymers that have too strong aggregation characteristics to match well with non-fullerene acceptors.

Conflicts of interest

There are no conflicts to declare.

Acknowledgements

This work was supported by the National Natural Science Foundation of China (51873227, 51503219, 51573205 and 51773220),

the Shandong Provincial Natural Science Foundation (ZR2015EQ002, ZR2017ZB0314), the Qingdao Applied and Fundamental Research (16-5-1-94-jch). X. Bao thanks the Youth Innovation Promotion Association CAS (2016194) for financial support. The authors thank beamline BL16B1 (Shanghai Synchrotron Radiation Facility) in GIWAXS test.

Notes and references

- G. Yu, J. Gao, J. C. Hummelen, F. Wudl and A. J. Heeger, *Science*, 1995, 270, 1789–1791.
- G. Li, V. Shrotriya, J. Huang, Y. Yao, T. Moriarty, K. Emery and Y. Yang, *Nat. Mater.*, 2005, 4, 864–868.
- A. C. Arias, J. D. MacKenzie, I. McCulloch, J. Rivnay and A. Salleo, *Chem. Rev.*, 2010, 110, 3–24.
- Y. Li, *Chem. – Asian J.*, 2013, 8, 2316–2328.
- J. K. Lee, W. L. Ma, C. J. Brabec, J. Yuen, J. S. Moon, J. Y. Kim, K. Lee, G. C. Bazan and A. J. Heeger, *J. Am. Chem. Soc.*, 2008, 130, 3619–3623.
- A. J. Heeger, *Adv. Mater.*, 2014, 26, 10–28.
- G. Zhang, J. Zhao, P. C. Y. Chow, K. Jiang, J. Zhang, Z. Zhu, J. Zhang, F. Huang and H. Yan, *Chem. Rev.*, 2018, 118, 3447–3507.
- A. Wadsworth, M. Moser, A. Marks, M. S. Little, N. Gasparini, C. J. Brabec, D. Baran and I. McCulloch, *Chem. Soc. Rev.*, 2019, 48, 1596–1625.
- J. Hou, O. Inganäs, R. H. Friend and F. Gao, *Nat. Mater.*, 2018, 17, 119.
- P. Cheng, G. Li, X. Zhan and Y. Yang, *Nat. Photonics*, 2018, 12, 131–142.
- Y. Lin, J. Wang, Z.-G. Zhang, H. Bai, Y. Li, D. Zhu and X. Zhan, *Adv. Mater.*, 2015, 27, 1170–1174.
- W. Wang, C. Yan, T.-K. Lau, J. Wang, K. Liu, Y. Fan, X. Lu and X. Zhan, *Adv. Mater.*, 2017, 29, 1701308.
- H. Yao, Y. Cui, R. Yu, B. Gao, H. Zhang and J. Hou, *Angew. Chem., Int. Ed.*, 2017, 56, 3045–3049.
- Y. Li, L. Zhong, B. Gautam, H.-J. Bin, J.-D. Lin, F.-P. Wu, Z. Zhang, Z.-Q. Jiang, Z.-G. Zhang, K. Gundogdu, Y. Li and L.-S. Liao, *Energy Environ. Sci.*, 2017, 10, 1610–1620.
- F. Liu, Z. Zhou, C. Zhang, J. Zhang, Q. Hu, T. Vergote, F. Liu, T. P. Russell and X. Zhu, *Adv. Mater.*, 2017, 29, 1606574.
- Y. Jia, Y. Zhang, W. Jiang, B. Su, C. Liu, E. Zhu and G. Che, *J. Mater. Chem. A*, 2019, 7, 10905–10911.
- J. Yuan, Y. Zhang, L. Zhou, G. Zhang, H.-L. Yip, T.-K. Lau, X. Lu, C. Zhu, H. Peng, P. A. Johnson, M. Leclerc, Y. Cao, J. Ulanski, Y. Li and Y. Zou, *Joule*, 2019, 3, 1140–1151.
- Y. Cui, H. Yao, L. Hong, T. Zhang, Y. Xu, K. Xian, B. Gao, J. Qin, J. Zhang, Z. Wei and J. Hou, *Adv. Mater.*, 2019, 31, 1808356.
- B. Fan, D. Zhang, M. Li, W. Zhong, Z. Zeng, L. Ying, F. Huang and Y. Cao, *Sci. China: Chem.*, 2019, 62, 746–752.
- L. Meng, Y. Zhang, X. Wan, C. Li, X. Zhang, Y. Wang, X. Ke, Z. Xiao, L. Ding, R. Xia, H.-L. Yip, Y. Cao and Y. Chen, *Science*, 2018, 361, 1094–1098.
- L. Han, N. Uranbileg, S. Jiang, Y. Xie, H. Jiang, Z. Lan, D. Yu, X. Bao and R. Yang, *J. Mater. Chem. A*, 2019, 7, 10505–10513.
- Y. Cai, L. Huo and Y. Sun, *Adv. Mater.*, 2017, 29, 1605437.
- H. Bin, Z. G. Zhang, L. Gao, S. Chen, L. Zhong, L. Xue, C. Yang and Y. Li, *J. Am. Chem. Soc.*, 2016, 138, 4657–4664.
- H. Zhou, L. Yang, A. C. Stuart, S. C. Price, S. Liu and W. You, *Angew. Chem., Int. Ed.*, 2011, 123, 3051–3054.
- D. Lee, S. W. Stone and J. P. Ferraris, *Chem. Commun.*, 2011, 47, 10987–10989.
- T. L. Nguyen, H. Choi, S. J. Ko, M. A. Uddin, B. Walker, S. Yum, J. E. Jeong, M. H. Yun, T. J. Shin, S. Hwang, J. Y. Kim and H. Y. Woo, *Energy Environ. Sci.*, 2014, 7, 3040–3051.
- Z. Li, K. Jiang, G. Yang, J. Y. L. Lai, T. Ma, J. Zhao, W. Ma and H. Yan, *Nat. Commun.*, 2016, 7, 13094.
- J. Li, Z. Liang, Y. Wang, H. Li, J. Tong, X. Bao and Y. Xia, *J. Mater. Chem. C*, 2018, 6, 11015–11022.
- J. Li, Y. Wang, Z. Liang, N. Wang, J. Tong, C. Yang, X. Bao and Y. Xia, *ACS Appl. Mater. Interfaces*, 2019, 11, 7022–7029.
- J. Mei and Z. Bao, *Chem. Mater.*, 2014, 26, 604–615.
- Y. Liu, J. Zhao, Z. Li, C. Mu, W. Ma, H. Hu, K. Jiang, H. Lin, H. Ade and H. Yan, *Nat. Commun.*, 2014, 5, 5293.
- D. Meng, D. Sun, C. Zhong, T. Liu, B. Fan, L. Huo, Y. Li, W. Jiang, H. Choi, T. Kim, J. Y. Kim, Y. Sun, Z. Wang and A. J. Heeger, *J. Am. Chem. Soc.*, 2016, 138, 375–380.
- W. Zhao, S. Li, H. Yao, S. Zhang, Y. Zhang, B. Yang and J. Hou, *J. Am. Chem. Soc.*, 2017, 139, 7148–7151.
- H. Zhang, H. Yao, J. Hou, J. Zhu, J. Zhang, W. Li, R. Yu, B. Gao, S. Zhang and J. Hou, *Adv. Mater.*, 2018, 30, 1800613.
- Y. Lin, F. Zhao, S. K. K. Prasad, J.-D. Chen, W. Cai, Q. Zhang, K. Chen, Y. Wu, W. Ma, F. Gao, J.-X. Tang, C. Wang, W. You, J. M. Hodgkiss and X. Zhan, *Adv. Mater.*, 2018, 30, 1706363.
- L. Gao, Z.-G. Zhang, H. Bin, L. Xue, Y. Yang, C. Wang, F. Liu, T. P. Russell and Y. Li, *Adv. Mater.*, 2016, 28, 8288–8295.
- H. Bin, L. Gao, Z.-G. Zhang, Y. Yang, Y. Zhang, C. Zhang, S. Chen, L. Xue, C. Yang, M. Xiao and Y. Li, *Nat. Commun.*, 2016, 7, 13651.
- S. Li, L. Ye, W. Zhao, S. Zhang, S. Mukherjee, H. Ade and J. Hou, *Adv. Mater.*, 2016, 28, 9423–9429.
- L. Han, W. Chen, T. Hu, J. Ren, M. Qiu, Y. Zhou, D. Zhu, N. Wang, M. Sun and R. Yang, *ACS Macro Lett.*, 2015, 4, 361–366.
- G. G. Malliaras, J. R. Salem, P. J. Brock and C. Scott, *Phys. Rev. B: Condens. Matter Mater. Phys.*, 1998, 58, R13411–R13414.
- D. Qian, L. Ye, M. Zhang, Y. Liang, L. Li, Y. Huang, X. Guo, S. Zhang, Z. A. Tan and J. Hou, *Macromolecules*, 2012, 45, 9611–9617.
- R. Heuvel, F. J. M. Colberts, M. M. Wienk and R. A. J. Janssen, *J. Mater. Chem. C*, 2018, 6, 3731–3742.
- S. Chen, Y. Liu, L. Zhang, P. C. Y. Chow, Z. Wang, G. Zhang, W. Ma and H. Yan, *J. Am. Chem. Soc.*, 2017, 139, 6298–6301.
- H. Hu, K. Jiang, G. Yang, J. Liu, Z. Li, H. Lin, Y. Liu, J. Zhao, J. Zhang, F. Huang, Y. Qu, W. Ma and H. Yan, *J. Am. Chem. Soc.*, 2015, 137, 14149–14157.
- L. Huo, T. Liu, X. Sun, Y. Cai, A. J. Heeger and Y. Sun, *Adv. Mater.*, 2015, 27, 2938–2944.

- 46 S. Zhang, Y. Qin, M. A. Uddin, B. Jang, W. Zhao, D. Liu, H. Y. Woo and J. Hou, *Macromolecules*, 2016, 49, 2993–3000.
- 47 A. K. K. Kyaw, D. H. Wang, V. Gupta, W. L. Leong, L. Ke, G. C. Bazan and A. J. Heeger, *ACS Nano*, 2013, 7, 4569–4577.
- 48 P. W. M. Blom, V. D. Mihailetschi, L. J. A. Koster and D. E. Markov, *Adv. Mater.*, 2007, 19, 1551–1566.
- 49 A. K. Kyaw, D. H. Wang, D. Wynands, J. Zhang, T. Q. Nguyen, G. C. Bazan and A. J. Heeger, *Nano Lett.*, 2013, 13, 3796–3801.
- 50 H. Li, Y. Zhao, J. Fang, X. Zhu, B. Xia, K. Lu, Z. Wang, J. Zhang, X. Guo and Z. Wei, *Adv. Energy Mater.*, 2018, 8, 1702377.